Electronic Supplementary Material (ESI) for Nanoscale.
This journal is © The Royal Society of Chemistry 2018

Electronic Supplementary Information

Intercalation of Aromatic Amine for the 2H-1T' Phase Transition of MoS_2 by Experiments and Calculations

Ik Seon Kwon,[a] In Hye Kwak,[a] Hafiz Ghulam Abbas,[b] Gabin Jung,[a] Yeron Lee,[a] Jeunghee Park,[,a] Seung Jo Yoo,[c] Jin-Gyu Kim,[c] and Hong Seok Kang*[,d]*

[a] Department of Chemistry, Korea University, Sejong 339-700, Korea,
E-mail: parkjh@korea.ac.kr

[b] Department of Nanoscience and Nanotechnology, Jeonbuk National University, Chonju, Chonbuk 560-756, Korea.

[c] Division of Electron Microscopic Research, Korea Basic Science Institute, Daejeon 305-806, Republic of Korea.

[d] Department of Nano and Advanced Materials, College of Engineering, Jeonju University, Chonju, Chonbuk 560-759, Korea, E-mail: hsk@jj.ac.kr

Contents

I. Experimental details: characterization

II. Supporting Tables.

Table S1. MoS_2 samples synthesized in the present work.

Table S2. Fitted parameters of EXAFS data.

Table S3. Composition of samples determined by elemental analysis.

Table S4. Lattice parameters of various configurations of (4×4) MoS_2 (**Item 1**: Structure optimization)

Table S5. Lattice parameters of optimized intercalated complexes.

Table S6. Calculated intercalation energy and charge transfer (**Item 2**: Analysis of the monotonic behavior of ΔQ vs. C_{Vs}).

Table S7. Impedance parameters from Nyquist plot and double-layer capacitance (C_{dl}).

Table S8. Comparison of HER performance.

III. Supporting Figures

Figure S1. SEM images.

Figure S2. XRD data.

Figure S3. XANES and EXAFS data.

Figure S4. XPS survey scan and fine-scanned Mo 3d, S 2p, and N 1s peaks.

Figure S5. NMR spectra.

Figure S6. XPS valence spectrum.

Figure S7. Raman spectrum.

Figure S8. TGA and DSC data.

Figure S9. Structures of (4×4) MoS_2.

Figure S10. Structures of (4×4) MoS_2-4DMPD and (4×4) MoS_2-6DMPD.

Figure S11. ESR data.

Figure S12. XPS of MS-12 after 6 months.

Figure S13. Chronoamperometric responses of HER.

Figure S14. Nyquist plots.

Figure S15. Cyclic voltammograms for evaluation of double-layer capacitance.

Figure S16. Mott-Schottky plots.

Figure S17. Total DOS of 1T' phase (4×4) MoS_2 and (4×4) MoS_2-4DMPD.

Figure S18. Total DOS of 2H and 1T' phase (4×4) MoS_2 with C_{Vs} = 0 and 12.5%.

IV. References

I. Experimental Details: characterization

The products were characterized by scanning electron microscopy (SEM, Hitachi S-4700), field-emission transmission electron microscopy (FE TEM, FEI TECNAI G2 200 kV, Jeol JEM 2100F, HVEM), energy-dispersive X-ray fluorescence spectroscopy (EDX), and electron energy-loss spectroscopy (EELS, GATAN GIF-2000). Fast Fourier-transform (FFT) images were generated by the inversion of the TEM images using Digital Micrograph GMS1.4 software (Gatan Inc.). High-resolution X-ray diffraction (XRD) patterns were obtained using the 9B and 3D beamlines of the Pohang Light Source (PLS) with monochromatic radiation (λ = 1.54595 Å). XRD pattern measurements were also carried out in a Rigaku D/MAX-2500 V/PC using Cu K_α radiation (λ = 1.54056 Å). XPS data were collected using the 8A1 beam line of the PLS with a photon energy of 600 eV

X-ray absorption near edge spectra (XANES) and X-ray extended X-ray absorption fine structure (EXAFS) spectra at the Mo K-edge were collected in transmission mode using the 10C beam line of the PLS with a ring current of 350 mA at 3.0 GeV. Energy calibration was carried out by simultaneously measuring the reference spectrum of Mo metal foil. Least-squares fits of EXAFS data were performed using the Athena and Artemis software packages, version 0.9.25.

Thermogravimetric analysis (TGA) and differential scanning calorimetry (DSC) measurements were performed using a Differential Scanning Calorimeter/Thermal Analyzer (Perkin Elmer DSC8000, Pyris 1TGA). The samples (10 mg) were heated from room temperature to 700 °C in a N_2 flow (100 sccm), at 10 °C/min. Elemental analysis were performed on a ThermoFisher Flash EA2000 analyzer. Raman spectra were measured with a micro-Raman spectrometer (Horiba ARAMIS IR2), using a diode laser with an excitation wavelength of 532 nm.

Electron spin resonance (ESR) measurements were performed on a Bruker EMX-Plus spectrometer at room temperature. The samples (4 mg) were loaded in a quartz tube. The

microwave frequency was 9.644564 GHz, and the microwave power was fixed to 20 mW to avoid saturation. The solid-state ^{13}C (100.64 MHz) NMR spectra were acquired on a Bruker AVANCE II^{+} 400 MHz NMR system (at the KBSI Seoul Western Center) equipped with a Bruker 3.2 mm bore HXY probe operating in HX mode. The magic angle spinning ^{13}C NMR experiments (one pulse method) were performed using a pulse length of 2 μs for a π/2 pulse length of 5 μs, and a pulse repetition delay time of 5 s. The spectra were referenced to an external adamantane standard in which the peak at higher chemical shift was set at 38.43 ppm. The spectra were processed using the Bruker Topspin software (version 3.2) using conventional techniques, and a 50 Hz line broadening window function was applied in all cases.

HER electrocatalysis (in 0.5 M H_2SO_4 electrolyte) was measured using a linear sweeping from 0 to −0.8 V (vs. RHE) with a scan rate of 2 mV s^{-1}. A saturated calomel electrode (SCE) was used as reference electrode, and a Pt wire was used as counter electrode. The Pt wire was shielded by a membrane that block the Pt ions to dissolve into the electrolyte. The electrolyte was purged with H_2 (ultrahigh grade purity) during the measurement. The applied potentials (E) reported in our work were referenced to the reversible hydrogen electrode (RHE) through standard calibration. In 0.5 M H_2SO_4 electrolyte (pH 0), E (vs. RHE) = E (vs. SCE) + E_{SCE} (= 0.241 V) + 0.0592 pH = E (vs. SCE) + 0.241 V. The overpotential (η) was defined as E (vs. RHE). The materials (0.39 mg cm^{-2}) were deposited on a glassy carbon rotating disk electrode (RDE), and a rotation speed of 1600 rpm was used for the linear sweep voltammetry (LSV) measurements.

Electrochemical impedance spectroscopy (EIS) measurements were carried out for the electrode in an electrolyte by applying an AC voltage of 10 mV in the frequency range of 100 kHz to 0.1 Hz at a bias voltage of -0.15 V (vs. RHE). To measure double-layer capacitance via CV, a potential range in which no apparent Faradaic processes occur was determined from static CV. This range is 0.1-0.2 V. All measured current in this non-Faradaic potential region is assumed to be due to double-layer capacitance. The charging current, i_c, is then measured from

CVs at multiple scan rates. The working electrode was held at each potential vertex for 10 s before beginning the next sweep. The double-layer capacitance current density (J) is equal to the product of the scan rate (ν) and the electrochemical double-layer capacitance (C_{dl}), as given by equation $J = \nu C_{dl}$, Thus, a plot of J as a function of ν yields a straight line with a slope equal to C_{dl}. The scan rates were 20-100 mV s^{-1}. Mott-Schottky (MS) analysis was performed at various frequencies: 5, 10, and 20 Hz. The MS curves were measured by cathodically sweeping the potential with an AC amplitude of 10 mV.

II. Supporting Tables

Table S1. Characteristics of 22 MoS_2 samples and corresponding growth conditions.

Sample No.	Sample Name	[DMPD]/ [$(NH_4)_2MoS_4$]	T (°C)[a]	[DMPD][b]	1T'[c]	Phase[d]	C_{Vs}[e]	Mo $3d_{5/2}$[f]
1	MS-0	0	220	0	0	2H	0	229.40
2		0.5	220	4	45	2H	13	228.83
3	MS-3	1	220	3	44	2H	13	228.90
4		2	220	7	45	1T'	11	228.59
5	MS-12	3	220	12	74	1T'	25	228.56
6		5	220	12	70	1T'	17	228.47
7		0.5	200	7	46	2H	9	228.83
8		1	200	7	45	2H	15	228.80
9		2	200	16	70	1T'	10	228.62
10		3	200	21	70	1T'	11	228.60
11		5	200	21	70	1T'	16	228.59
12		0.5	180	8	50	2H	5	228.87
13		1	180	10	50	2H	8	228.77
14		2	180	16	64	1T'	12	228.61
15	MS-22	3	180	22	63	1T'	8	228.49
16		5	180	22	74	1T'	16	228.51
17		0.5	160	12	48	2H	1	228.90
18		1	160	13	49	2H	6	228.85
19		2	160	22	66	1T'	5	228.54
20		3	160	22	70	1T'	9	228.57
21	MS-33	5	160	33	70	1T'	4	228.45
22		3	140	40	67	1T'	0	228.51

[a] Temperature of hydrothermal reaction.
[b] Concentration (%) of intercalated DMPD ([DMPD]/[MoS_2]) determined using XPS data (N 1*s* and Mo 3*d* peaks).
[c] Fraction (%) of the 1T'-phase MoS_2 determined using Mo 3d XPS peak.
[d] Main phase, based on the highest fraction among 2H and 1T' phases.
[e] Concentration (%) of S vacancies (= 0.5×[S]/[Mo]) determined using S 2p and Mo 3d XPS peaks.
[f] Mo $3d_{5/2}$ peak position (eV) of the 1T' phase (2H phase in the case of MS-0).

Table S2. Fitted parameters of EXAFS data for MS samples.

Sample	Scattering Path	R (Å)[a]	CN[b]	ΔE (eV)[c]	σ^2 (Å^2)[d]
bulk MoS_2	Mo-S	2.41	6.0	1.3	0.0025
	Mo-Mo	3.17	6.0	0.9	0.0030
MS-0	Mo-S	2.40	6.2 ± 0.3	2.7	0.0028
	Mo-Mo	3.16	4.2 ± 0.1	2.6	0.0036
MS-3	Mo-S	2.39	6.4 ± 0.4	-3.2	0.0091
	Mo-Mo	2.76	1.7 ± 0.5	2.2	0.0082
MS-12	Mo-S	2.40	6.5 ± 0.4	-2.3	0.0092
	Mo-Mo	2.76	1.6 ± 0.4	2.3	0.0076
MS-22	Mo-S	2.40	6.4 ± 0.4	-1.2	0.0090
	Mo-Mo	2.76	1.8 ± 0.5	3.2	0.0087
MS-33	Mo-S	2.39	7.0 ± 0.5	-3.9	0.0101
	Mo-Mo	2.76	2.0 ± 0.6	2.1	0.0096

[a] Distance between scattering atoms.
[b] Coordination number of Mo atoms.
[c] Edge energy shift, representing between the energy grids of experimental and theoretical data.

[d] Debye-Waller factor.

Table S3. Composition of selected samples determined by elemental analysis.

Sample Name	Temp. (°C)[a]	[H]	[C]	[N]	[S]	[O]	[DMPD]/[MoS_2][b]
MS-0	220	30.9	2.8	0.5	44.6	21.2	2.2%
MS-3	220	35.3	13.5	1.6	39.4	10.1	4.1%
MS-12	220	38.4	25.5	3.2	25.2	7.6	12%
MS-22	180	38.2	30.9	4.5	21.0	5.4	21%
MS-33	160	38.5	33.3	6.2	18.3	3.7	34%

[a] Synthesis temperature.

[b] Concentration of [DMPD] calculated using the [N]/[S] ratio. NH_4^+ intercalation could occur in the MS-0 sample.

Table S4. Lattice parameters (*a, b* and *c*) of various configurations of the (4×4) MoS_2 in the 1T' (and 1T, 1T") and 2H phases with different number of S vacancies (N_{Vs}). The structure optimizations of the 1T' and 1T" phases are discussed in **Item 1**.

N_{Vs} (C_{Vs})[a]	Phase	Configurations	*a, b, c* (Å), and γ[b]	$l_{V_S-V_S}$ (Å)[c]	l_{Mo-Mo} (Å)[d]	E_{rel} (eV)[e]
0	2H	A_0	12.64, 12.64, 12.53, 120° (3.16)	-	3.16, 3.16	0.00
	1T	A_0	12.56, 12.56, 12.53,120° (3.14)	-	3.17, 3.17	26.77
	1T'	A_0	13.10, 12.72, 12.52, 119° (6.55, 3.18)		2.77, 3.18	18.47
	1T"	A_0	12.88, 12.88, 12.52, 119.5° (6.44)	-	2.78, 3.23	20.01
3 (4.7%)	2H	A_3	12.54, 12.54, 12.53, 120° (3.14)	3.92, 3.92	3.16, 3.16	0.00
		B_3	12.54, 12.54, 12.53, 120° (3.14)	-	3.16, 3.16	0.43
	1T'	A_3	13.05, 12.64, 11.90, 119° (6.53, 3.16)	3.17, 3.17	2.76, 3.15	13.95
		B_3	13.05, 12.64, 11.90, 119° (6.53, 3.16)	3.19, 3.19	2.76, 3.16	14.36
	1T"	A_3	12.88, 12.88, 12.53, 119.5° (3.22)	3.17, 3.17	2.74, 3.24	14.90
		B_3	12.88, 12.88, 12.53, 119.5° (3.22)	3.19, 3.19	2.74, 3.24	15.82
6 (9.4%)	2H	A_6	12.60, 12.60, 12.53, 120° (3.15)	3.95, 5.05	3.16, 3.16	0.00
		A_6	12.60, 12.60, 12.53, 120° (3.15)	4.76, 5.78	3.16, 3.16	0.32
	1T'	A_6	12.98, 12.65, 12.91, 119° (6.49, 3.16)	4.11, 5.32	2.78, 3.19	10.55
		B_6	12.98, 12.65, 12.91, 119° (6.49, 3.16)	4.76, 5.78	2.76, 3.19	11.08
	1T"	A_6	12.76, 12.76, 12.53, 119.5° (3.19)	3.95, 5.05	2.78, 3.23	12.66
		B_6	12.76, 12.53, 119.5° (3.19)	4.76, 5.78	2.77, 3.24	12.70
13 (20.3%)	2H	A_{13}	12.60, 12.60, 12.53, 120° (3.15)	3.95, 5.05	-	0.00
		B_{13}	12.60, 12.53, 120° (3.15)	3.20, 3.41	-	0.14
	1T'	A_{13}	12.60, 12.48, 12.33, 119° (6.30, 312)	3.10, 3.12	-	2.39
		B_{13}	12.60, 12.48, 12.33, 119° (6.30, 3.12)	3.20, 3.41	-	3.79
		A_{13}	12.64, 12.64. 12.33,	3.10, 3.12	-	4.29

			119.5° (3.16)			
		B_{13}	12.64, 12.64, 12.33, 119.5° (3.16)	3.20, 3.41	-	5.46
19 (29.7%)	1T'	A_{19}	12.68, 11.70, 12.44, 119° (6.34, 2.93)	2.97, 3.03	-	0.00
	1T"	A_{19}	12.60, 12.60, 12.53, 119.5° (3.15)	2.97, 3.03	-	1.03
	2H	A_{19}	12.54, 12.54, 12.53, 120° (3.14)	-	-	4.25

[a] The number in parentheses denote the concentration of S vacancies (C_{Vs}).
[b] Lattice constants of a 4×4 supercell configuration. The lattice constant a (= b) of the 2H and 1T" phase unit cell (shown in parentheses) was calculated as a/4 and a/2, respectively. The lattice constants a and b of the 1T' phase unit cell (also shown in parentheses) were calculated as a/2 and b/4, respectively. The angles (γ) between the a and b axes are also shown.
[c] Two shortest distances between two S vacancies at different MoS_2 layers.
[d] Two shortest distances between adjacent Mo and Mo atoms. A large variation occurs for $N_{Vs} > 6$.
[e] Relative energy, defined as the total energy of each configuration minus that of the most stable configuration A_i.

Item 1. Structure optimization process for the 1T' and 1T'' phases.

In the case of the 1T' phase, the structure optimizations involved three steps. In the first step, the a (= b) and c constants were optimized assuming that MoS_2 adopted the 1T phase for each C_{Vs} value. We considered more than three configurations in which the S vacancies are distributed with different ways. In the following, the most stable configuration is labeled A_i and the others are denoted B_i and C_i, in order of stability. The second step involved further optimizations to allow all lattice parameters (including the angles) to relax freely, in such a way to minimize both forces and stresses under a restriction of $a = b$, resulting in the 1T" phase. In the last step, the lattice constants ($a \neq b$) were manually adjusted until optimal values were obtained. The final result is that all configurations adopt the 1T' phase. We do not find any case that the stability order between A_i and B_i is altered after the last two steps. In the case of the S vacancy-free configuration, the 1T' phase is significantly more stable (1.54 eV) than the 1T" one.

Table S5. Lattice parameters of MoS_2 intercalated with DMPD molecules.

N_{Vs} (C_{Vs})[a]	[DMPD](%)[b]	2H *a, c* (Å)[c]	1T' *a, b, c* (Å)[d]
0	0	12.64, 12.53	13.10, 12.72, 12.90
	12.5	12.64, 20.50	13.10, 12.72, 19.45
	18.8	12.64, 26.00	13.10, 12.72, 25.74
3 (4.7%)	0	12.54, 12.32	13.05, 12.64, 11.90
	18.8	12.54, 25.20	13.05, 12.64, 25.13
6 (9.4%)	0	12.60, 12.53	12.98, 12.65, 12.91
	12.5	12.64, 20.00	12.98, 12.65, 19.54
	18.8	12.60, 25.50	12.98, 12.65, 26.04
13 (20.3%)	0	12.60, 12.53	12.60, 12.48, 12.33
	12.5	12.60, 19.39	12.55, 12.42, 19.37
19 (29.7%)	0	12.54, 12.53	12.68, 11.70, 12.44
	12.5	12.54, 19.50	12.39, 11.68, 20.19

[a] Number and concentration (in parentheses) of S vacancies.
[b] Concentration of DMPD in parentheses.
[c] Lattice constants of a 4×4 supercell configuration of the 2H phase. The lattice constant *a* of unit cell (shown in in parentheses) corresponds to is *a*/4 of the supercell.
[d] Lattice constants of a 4×4 supercell configuration of the 1T' phase. The lattice constants *a* and *b* of unit cell (shown in in parentheses) correspond to *a*/2 and *b*/4 of the supercell, respectively. The angle between the *a* and *b* axes is 119°.

Table S6. Intercalation energy and charge transfer in the DMPD-MoS_2 intercalated complexes.

Guest[a]	N_{Vs} (C_{Vs})[b]	Stable Phase	E_{ic} (eV)[c]		ΔQ (e)[d]	
			2H	1T'	2H	1T'
4DMPD (12.5%)	0	2H	-0.19	-0.45	0.18	1.32
	6 (9.4%)	2H	-0.26	-0.94	0.62	0.97
	13 (20.3%)	1T'	-0.23	-1.30	0.68	0.85
	19 (29.7%)	1T'	-0.48	-1.44	0.68	0.70
6DMPD (18.8%)	0	2H	0.35	-0.40	0.21	1.35
	3 (4.7%)	2H	-0.11	-0.18	0.60	1.15
	6 (9.4%)	1T'	-0.23	-0.67	0.75	1.15

[a] Concentration of DMPD in parentheses.
[b] Number and concentration (in parentheses) of S vacancies.
[c] Intercalation energy per DMPD.
[d] Total charge transfer from $m/2$ DMPD molecules to a MoS_2 layer.

The E_{ic} was defined as the average energy change per DMPD molecule in the following process: (4×4) MoS_2 + mDMPD → (4×4) MoS_2-mDMPD. In particular, E_{ic}=[E{(4×4) MoS_2-mDMPD}-E{(4×4) MoS_2}-E{mDMPD}]/m. The energy of mDMPD is assumed to be (m/2) times the total energy of two interacting DMPD molecules in the most stable configuration.

The ΔQ of the 1T' phase creases monotonically with increasing the C_{Vs} at a fixed DMPD concentration: starting from a high initial value, Q shows a rapid decrease followed by a more gradual further decline. The 2H phase shows the opposite behavior: the initial ΔQ is smaller than in the 1T' phase, and then shows a rapid increase followed by a slower further increase. If ΔQ did *not* display a monotonic behavior vs. C_{Vs} but remained constant at its initial value (corresponding to C_{Vs} = 0) instead, then the phase transition would be observed at a much *lower* C_{Vs}, which would not be consistent with the present experimental results. Therefore, it is important to determine the origin of the monotonic behavior of the ΔQ vs. C_{Vs} curves for both phases. The following section (**Item 2**) provides a detailed analysis of this aspect in terms of electronic structure, showing that the monotonic decrease observed for the 1T' phase can be ascribed to the decrease in the polarizability of the MoS_2 monolayer as C_{Vs} increases, whereas the 2H phase shows the exact opposite trend.

Item 2. Analysis of the monotonic behaviors of ΔQ vs. C_{Vs} in the two phases at a fixed DMPD concentration.

The result can be understood in terms of the electronic structure of the MoS_2 monolayer in the two phases, rather than in the bulk. In this sense, the present analysis has no direct correlation with the intercalation energy of DMPD, whose reference state is the three dimensional (3D) MoS_2 crystal. This is because the interlayer distance of the MoS_2-*m*DMPD complex is so large (~20.50 Å, see **Table S5**) that the charge transfer is governed by the interaction of the monolayer with DMPD. We recall that Perdew-Burke-Ernzerhof (PBE) calculations showed that the defect-free monolayer is still a semiconductor with an appreciable band gap (1.68 eV) in the 2H phase, whereas it shows metallic behavior in the 1T' phase, with more than one band crossing the Fermi level.[S1] Therefore, significant differences can be expected between the polarizabilities of the defect-free monolayer in the two phases. When the monolayer forms a complex with DMPD molecules, the charge density that can be accommodated in the monolayer will also be significantly different in the two phases. **Figures Ia** and **Ib** (see below) show the band structures obtained from our PBE calculations.

On the other hand, vacancies introduce defect states around the Fermi level of the material. These states appear to have opposite effects on the polarizability of the two phases. In the 2H phase, the defective states are expected to enhance the polarizability of the material. As **Figure Ic** shows, this is because these states are interspersed within the band gap of the defect-free MoS_2 monolayer, in such a way that the gap is reduced, increasing the polarizability of the material. In the 1T' phase, as the vacancy concentration increases, an increasing number of localized states replace the delocalized states near the Fermi level (see **Figure Id**). In short, the monotonic decrease of ΔQ vs. C_{Vs} in the 1T' phase can be ascribed to the decrease of the polarizability of the MoS_2 monolayer, whereas the opposite may be true for the 2H phase.

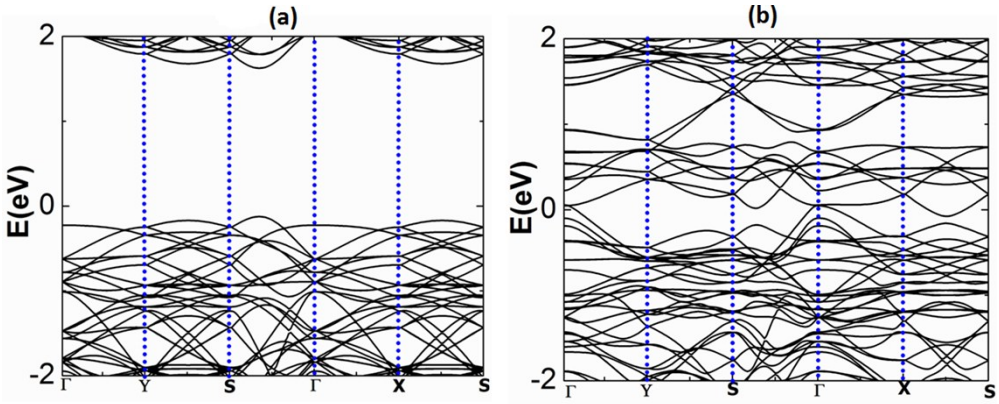

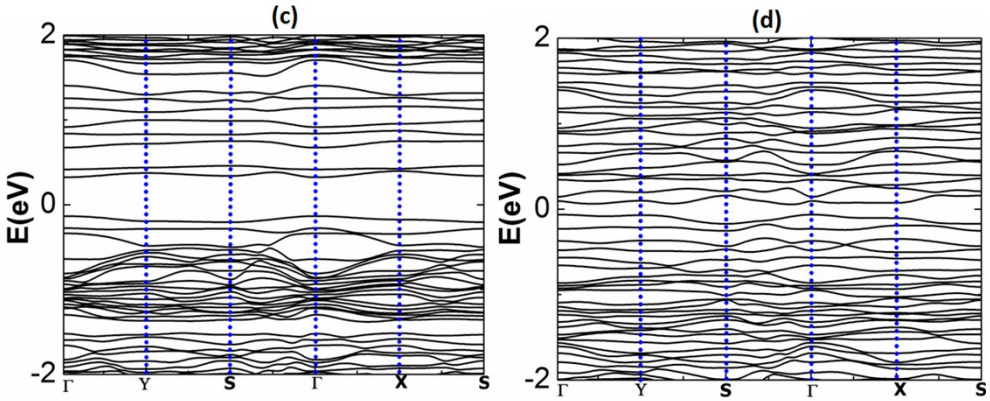

Figure I. PBE band structures of the (4×4) MoS_2 monolayer structure in the (a) 2H and (b) 1T' phase at C_{Vs} = 0% and the (c) 2H and (d) 1T' phases at C_{Vs} = 12.5%.

Table S7. Impedance parameters for the equivalent circuit that was shown in **Figure S14**, and the double-layer capacitance (C_{dl}) (**Figure S15**).

Samples	Electrochemical impedance spectroscopy		C_{dl} (mF cm^{-2})
	R_s (Ω)	R_{ct} (Ω)	
MS-0	9.07	910.8	18.6
MS-3	8.11	38.5	51.2
MS-12	7.01	36.5	62.0
MS-22	7.84	92.4	30.0
MS-33	9.15	118.9	27.0

Table S8. Comparison of HER performance (in pH 0) of MoS_2 in the literatures.

Reference	Materials	Phase	$E_{J=10}$ (mV) at 10 mA cm^{-2}	Tafel slope (mV dec^{-1})
S2	Defect-rich MoS_2 nanosheet	2H	190	50
S3	Conducting MoS_2	1T	200	40
S4	Oxygen-Incorporated MoS_2	2H	187	55
S5	Edge-terminated MoS_2 nanosheet	2H	149	49
S6	Strained MoS_2 nanosheet	2H	170	60
S7	Ammoniated MoS_2	1T	320	45
S8	1T MoS_2 single-layer nanosheets	1T	N/A	45
S9	Metallic phase MoS_2 nanosheet	1T	175	41
S10	1T MoS_2 nanosheet	1T	154	43
S11	Ammonia-MoS_2	N/A	200	55
S12	ALD-MoS_2	2H	N/A	79
S13	1T' MoS_2 monolayer	1T'	300	83
S14	1T/2H MoS_2	1T/2H	234	46
S15	Zn- MoS_2	2H	N/A	51
S16	Functionalized metallic MoS_2 nanosheet	1T	348	75
S17	1T MoS_2 nanodot	1T	173	53
Present work	DMPD-intercalated MoS_2 (MS-12)	1T'	160	38

N/A: Not applicable

III. Supporting Figures

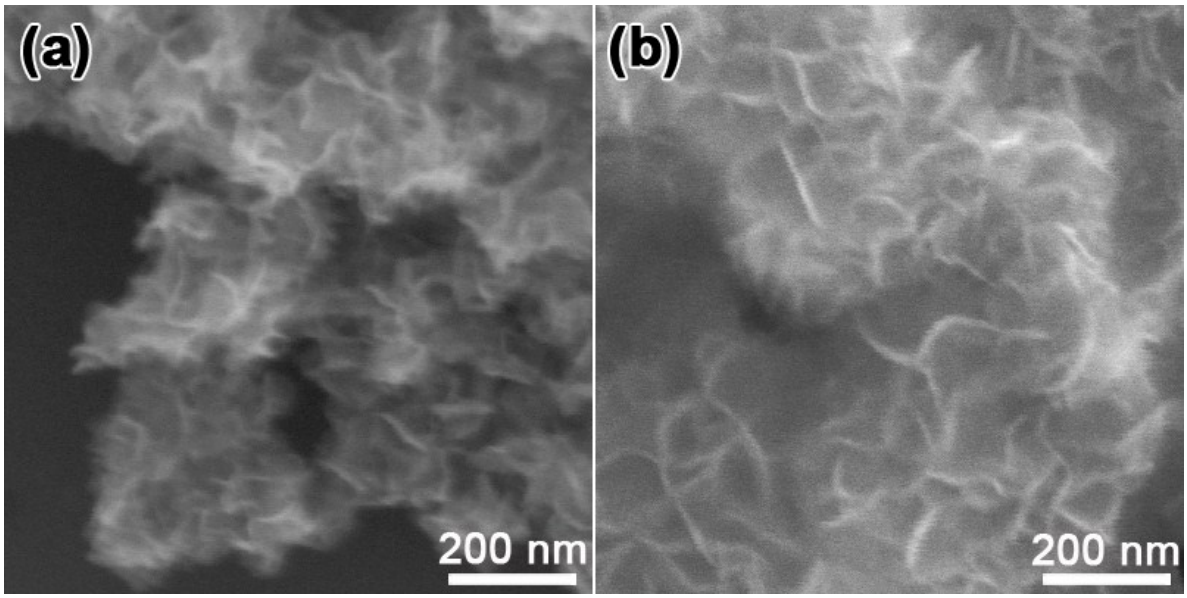

Figure S1. Scanning electron microscopy images of MS-0 and MS-12.

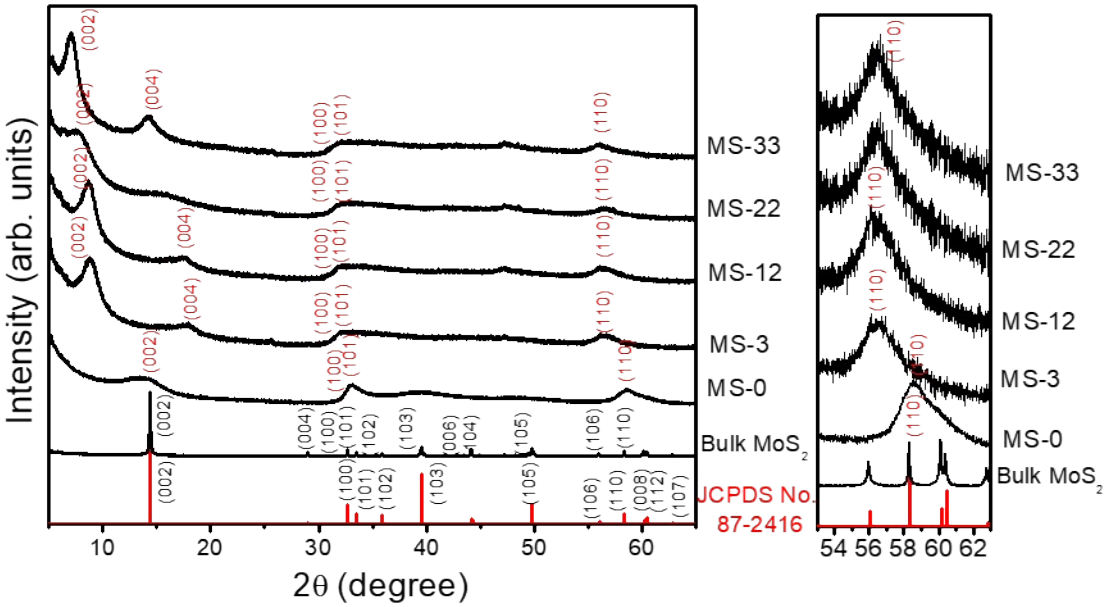

Figure S2. XRD patterns of bulk MoS_2 (powders) and MS samples (MS-0, MS-3, MS-12, MS -22, MS-33). The peaks were referenced to those of the 2H phase MoS_2 (JCPDS No. 87-2416; a = 3.160 Å and c = 12.290 Å). The magnified (110) peaks are shown on the right.

The peaks of all samples were referenced to those of the hexagonal (2H) phase of bulk MoS_2 (JCPDS No. 87-2416; a = 3.160 Å and c = 12.290 Å). In the case of MS-0, the (002) peak at 2θ = 13.8° corresponds to a distance between (002) planes (d_{002}) of 6.5 Å (calculated using Bragg's law), which is larger than that of 2H-MoS_2 (6.15 Å), probably due to the intercalation of water and/or ammonium ions. The 2θ position of (110) peak is 58.6°, indicating the lattice constant a = 3.16 Å.

The (002) peaks of the MS-3, MS-12, MS-22, and MS-33 are shifted to lower 2θ angles of 8.8°, 8.6°, 7.8°, and 7.0°, respectively, indicating that the intercalation leads to a significant increase in the corresponding d_{002} spacings, to 10.0, 10.3, 11.3, and 12.6 Å, respectively. Therefore, the c (= $2\times d_{002}$) constant increases with increasing DMPD concentration. The (110) peaks of the MS-3, MS-12, MS-22, and MS-33 are shifted to lower 2θ angles of 56.4°, 56.3°, 56.1°, and 56.0°, respectively. The lattice constant a is calculated to be 3.27-3.28 Å, using the position of (110) peak.

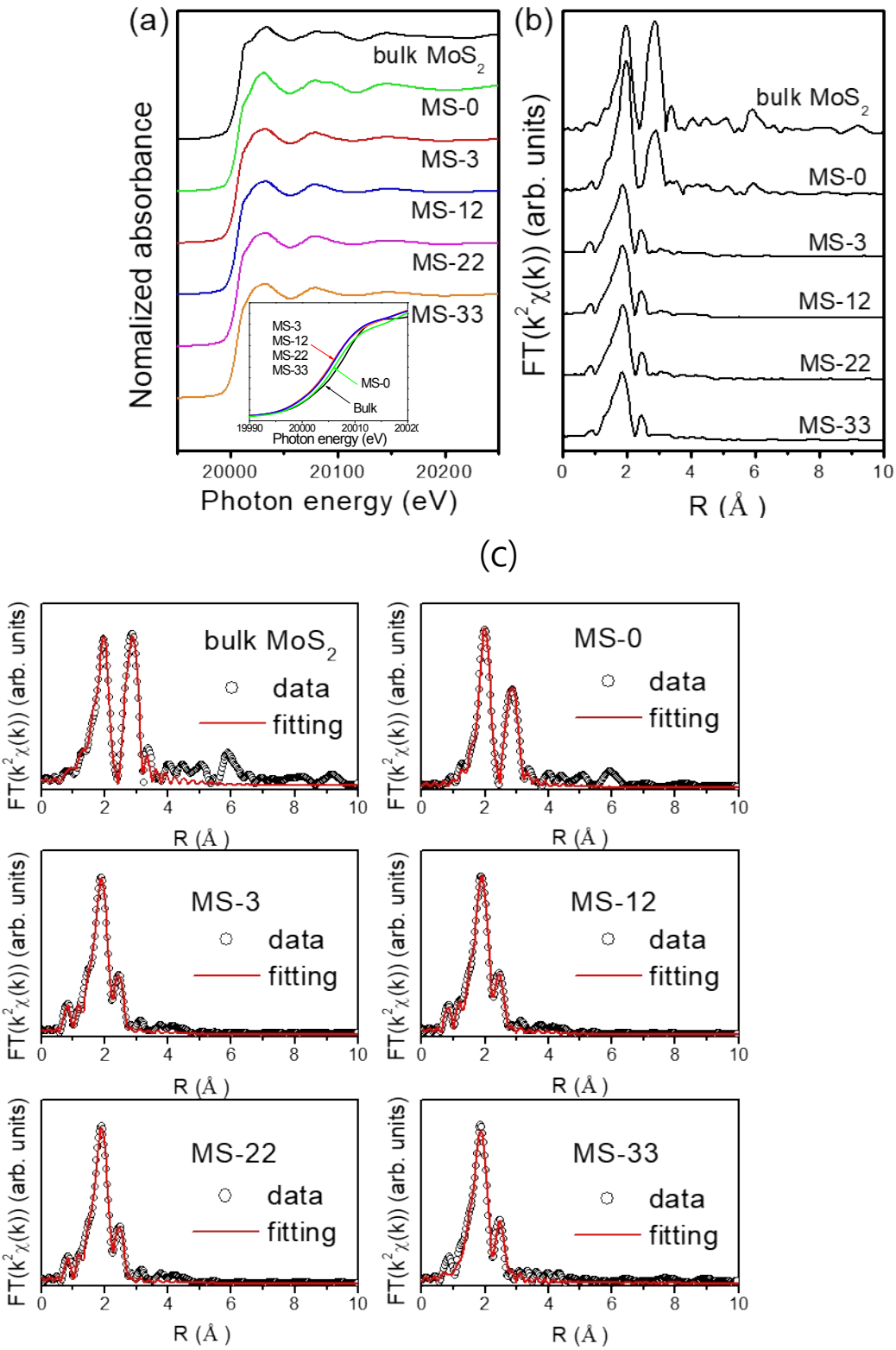

Figure S3. (a) XANES and (b) Fourier-transformed EXAFS spectra at the Mo K edge for bulk MoS_2 and MS samples (MS-0, MS-3, MS-12, MS-22, and MS-33), and (c) corresponding fitting curves.

(a) The evolution of the local crystal structure of MoS_2 upon the intercalation of DMPD was probed with Mo K-edge X-ray absorption near edge spectra (XANES) analysis. The spectrum of bulk MoS_2 is also displayed as a reference. The edge energies of all DMPD-MoS_2 complexes are lower than those of unintercalated MoS_2 (MS-0) and bulk MoS_2 (inset). It suggests that the intercalation of DMPD molecules induces more metallic states of Mo.

(b) The EXAFS peaks of the fine X-ray absorption spectra above the Mo K-edge was Fourier transformed (FT). The peaks in the FT profiles (in real space) denote the distances between nearest-neighbor atoms. The significant differences between the profiles of the DMPD-intercalated and MS-0 (and bulk MoS_2) samples suggest a marked difference in the local atomic arrangements.

(c) The FT curves were fitted to two scattering paths. The fitting parameters are summarized in **Table S2**. Least-squares fits of EXAFS data were performed using the ARTEMIS module of the IFEFFIT and USTCXAFS software packages. The FT curves of 2H-phase MS-0 and bulk MoS_2 are characterized by two main peaks at 2.40-2.41 and 3.16-3.17 Å, corresponding to the nearest Mo-S and Mo-Mo bonds, respectively.[S18,S19] In contrast, the FT curves of the intercalated MS samples reveal a noticeable shift to 2.76 Å in the peak related to the nearest Mo-Mo bonds. Our calculations showed that the shortest Mo-Mo distances in the 2H and 1T' phases are 3.16–3.18 Å and 2.76–2.78 Å, respectively (see **Table S4**). Therefore, we conclude that the DMPD-intercalated samples adopt a distorted octahedral coordination of the 1T' phase. The Debye-Waller factor, which accounts for the static and thermal disorder, is larger for the intercalated samples than for the MS-0 and bulk MoS_2, suggesting that the intercalation of DMPD produces a broad range of Mo-S and Mo-Mo distances in the 1T' phase.

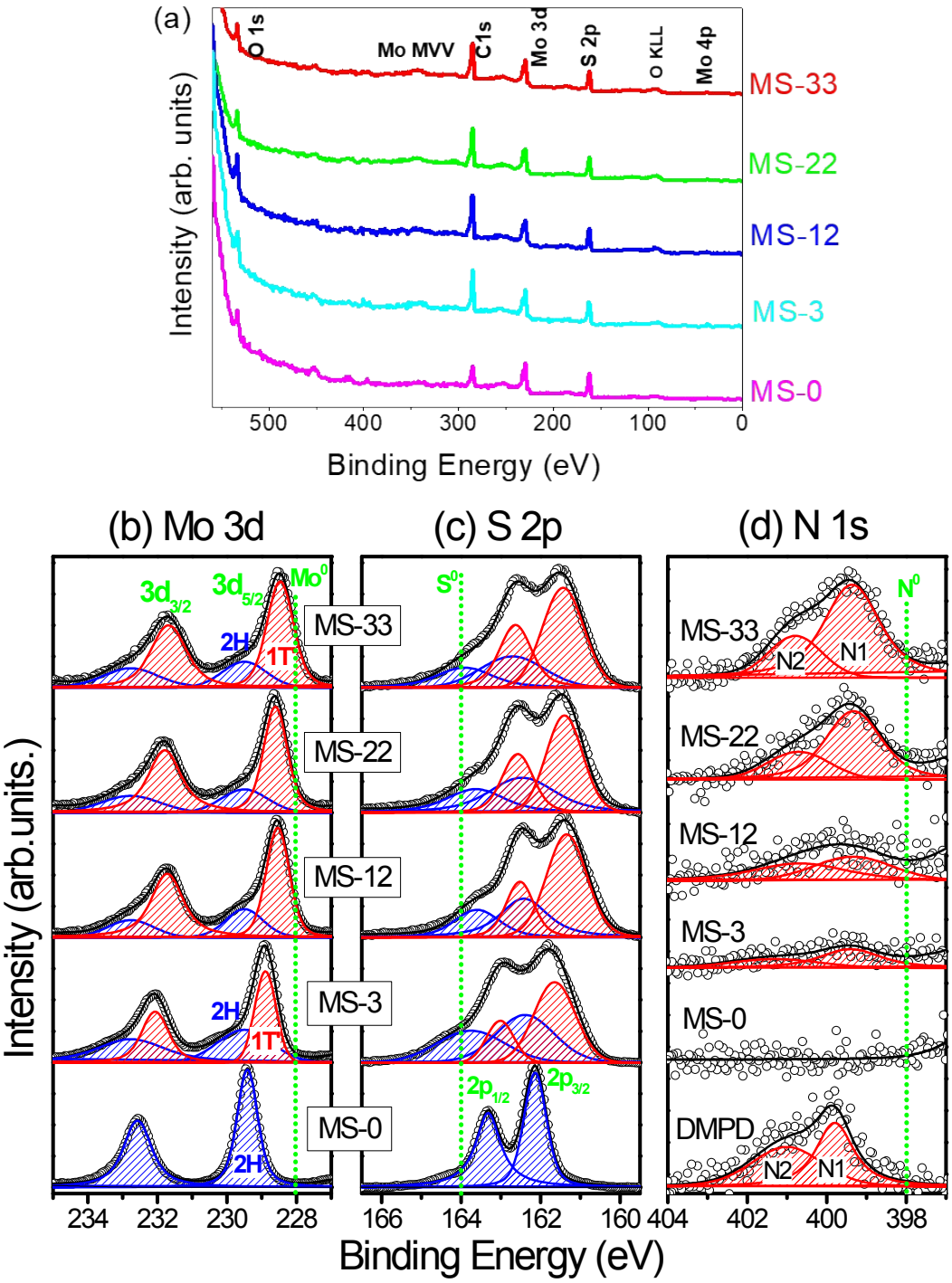

Figure S4. (a) XPS survey spectra of MS-0, MS-3, MS-12, MS-22, and MS-33. The photon energy is 600 eV. Fine-scan (b) Mo 3d, (c) S 2p, and (d) N 1s peaks. The experimental data (open circles) are fitted by a Voigt function, and the sum of the resolved bands is represented by a black line. The positions of the peaks corresponding to neutral species ($3d_{5/2}$ of Mo^0, $2p_{3/2}$ of S^0, and N^0) are marked by dotted lines to highlight the corresponding shift.

Figure S4a shows the XPS survey spectra of MS-0, MS-3, MS-12, MS-22, and MS-33. The C peak of MS-3, MS-12, MS-22, and MS-33 is larger than that of MS-0, due to the DMPD molecules. **Figures S4b**, **S4c**, and **S4d** shows fine-scanned XPS spectra of the Mo 3d, S 2p, and N 1s regions, respectively. The peaks were resolved using a Voigt function, in order to identify the corresponding bonds. **Figure S4a** shows the Mo $3d_{3/2}$ and $3d_{5/2}$ peaks (separated by about 3 eV). The fraction of 1T' phase, as determined from the area of two bands (red and blue), was 44% for MS-3, 74% for MS-12, 63% for MS-22, and 70% MS-33. As [DMPD] increases to 12%, the fraction of 1T' phase becomes 70%.

Figure S4c shows the S $2p_{3/2}$ and S $2p_{1/2}$ peaks, which are separated by about 1.2 eV. The MS-0 sample shows peaks at 162.1 and 163.3 eV, which are 1.9 eV red-shifted with respect to the signal of neutral S (S^0) at 164.0 and 165.2 eV. They correspond to the S^{2-} anions bonded with the Mo cations in the 2H phase. For the DMPD-intercalated samples, the broad peak was resolved into four bands; two each for the 2H phase (blue) and the 1T' phase (red). The larger red-shift bands are assigned to those of electron-rich 1T' phase.

Figure S4d shows the N 1s peak for the intercalated MoS_2 samples and DMPD powders. The background at lower energies is due to the Mo $3p_{3/2}$ peak at ~395 eV (c.f., Mo $3p_{31/2}$ peak at ~412 eV). In the case of the DMPD powders, the peak was resolved into two bands at 400 eV (N1 band) and 401 eV (N2 band), which are blue-shifted with respect to the signal of neutral N (N^0) at 398.1 eV. The ratio of N1 and N2 band is close to 1, so the N1 and N2 bands are assigned to N-C and N-H bonds, respectively. In the intercalated MoS_2, Ni and N2 bands of DMPD molecules appear at ~400 and ~401 eV, respectively, which are similar with those of DMPD powders. The width increases significantly compared to the DMPD powders, suggesting non-homogenous electrostatic interaction with the MoS_2 layers.

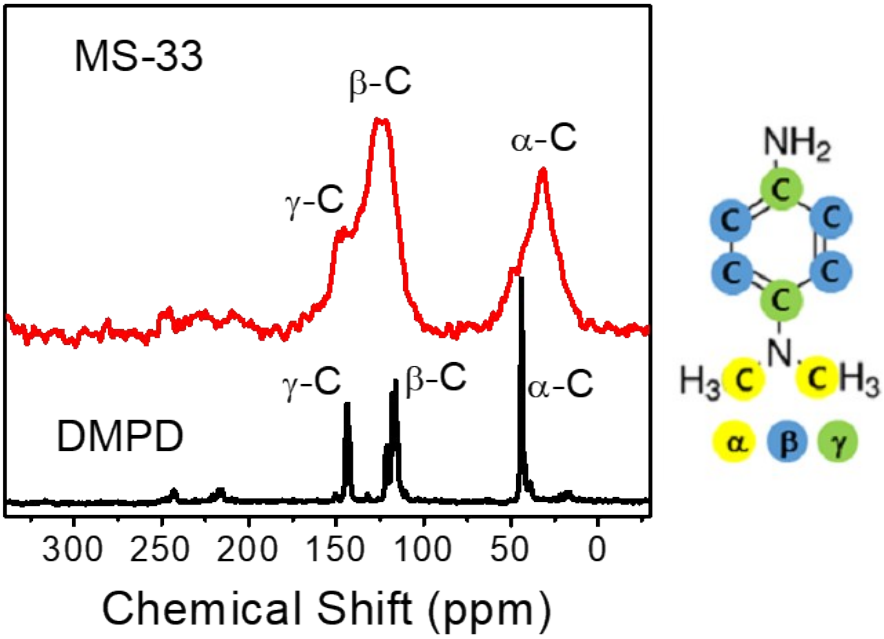

Figure S5. Solid-state ^{13}C NMR spectra of DMPD powders and MS-33 sample.

In the NMR spectrum of the DMPD powders, the α-C ($(CH_3)_2$-N-), β-C (C-C=C), and γ-C (> C-N) peaks are located at 44, 118, and 144 ppm, respectively. The α-C, β-C, and γ-C peaks appear at 30, 124, and 143 ppm, respectively, indicating that the DMPD molecules exist in MoS_2. The peak broadening is probably due to the non-homogenous electrostatic interaction with MoS_2.

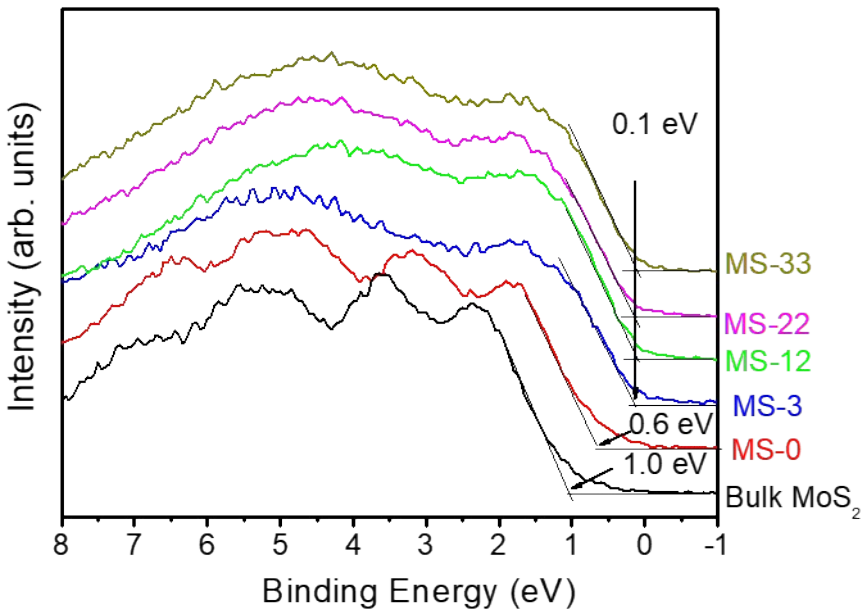

Figure S6. XPS valence band spectra of bulk MoS_2 (powders) and MS samples (MS-0, MS-3, MS-12, MS-22, and MS-33).

The positions of the valence band maximum were evaluated by linear extrapolation of the onset of the XPS valence band spectra. The binding energies were calibrated using the work function of Au metal foil. The valence band maxima of the 2H-phase bulk MoS_2, and MS-0 are 1.0 and 0.6 eV, respectively. Upon DMPD intercalation, the valence band maxima are red-shifted to 0.1 eV, which supports the formation of the metallic 1T' phase.

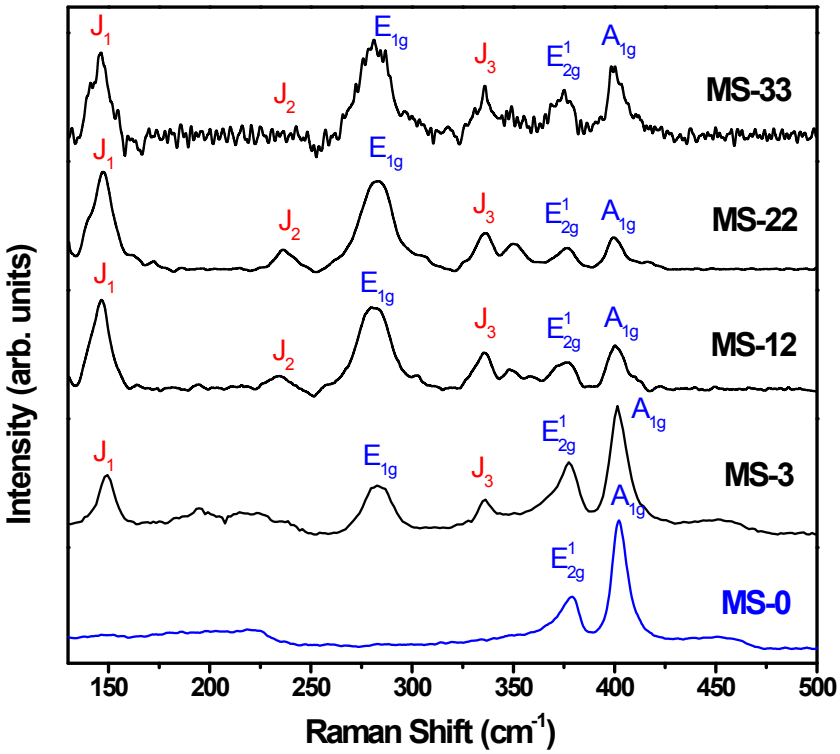

Figure S7. Raman spectra of MS-0, MS-3, MS-12, MS-22, and MS-33, measured using a diode laser with an excitation wavelength of 532 nm.

MS-0 exhibit the characteristic Raman peaks of the 2H phase at 378 cm^{-1} and 402 cm^{-1}, corresponding to in-plane E^1_{2g} and out-of-plane A_{1g} vibration modes, respectively. The Raman spectrum of the DMPD-intercalated samples shows three typical peaks of the 1T' phase, i.e., the J_1 peak at 146 cm^{-1}, the J_2 peak at 235 cm^{-1}, and the J_3 peak at 336 cm^{-1}, as well as the E_g vibrational mode at 283 cm^{-1}. [S20]

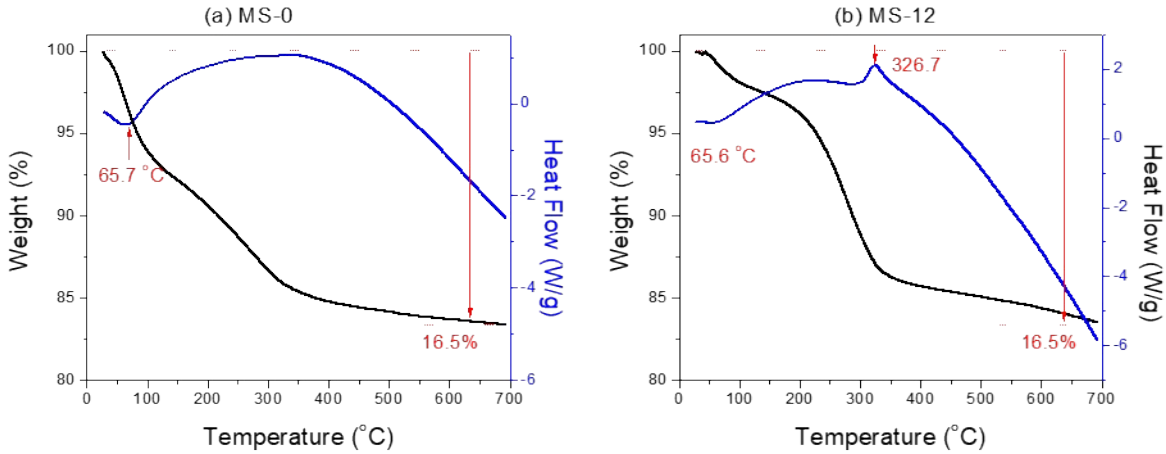

Figure S8. TGA and DSC data of (a) MS-0 and (b) MS-12. The samples were heated from room temperature to 700 °C at 10 °C/min and under N_2 flow (100 sccm).

The TGA curve of MS-0 shows a total weight loss of 16.5% at 700 °C, which can be divided into partial losses of 7% at 25–100 °C, 8% at 100–340 °C, and 1.5% between 340 and 700 °C. The DSC curve shows an endothermic peak at 65.7 °C, corresponding to the first weight loss step, which is ascribed to the release of adsorbed species such as water. The second weight loss of 10% is probably due to the intercalated water of NH_4^+ ions that originated from the precursors.

On the other hand, MS-12 shows weight losses of 2% in the 25–100 °C range, 12% at 100-350 °C, and 2.5% between 350 and 700 °C, with a total weight loss of 16.5%. The DSC curve shows an endothermic peak at 65.6 °C, corresponding to the release of adsorbents. An exothermic peak, not observed for MS-0, emerges at 326.7 °C. This peak could be due to the transformation from the 1T' to the 2H phase.[S21]

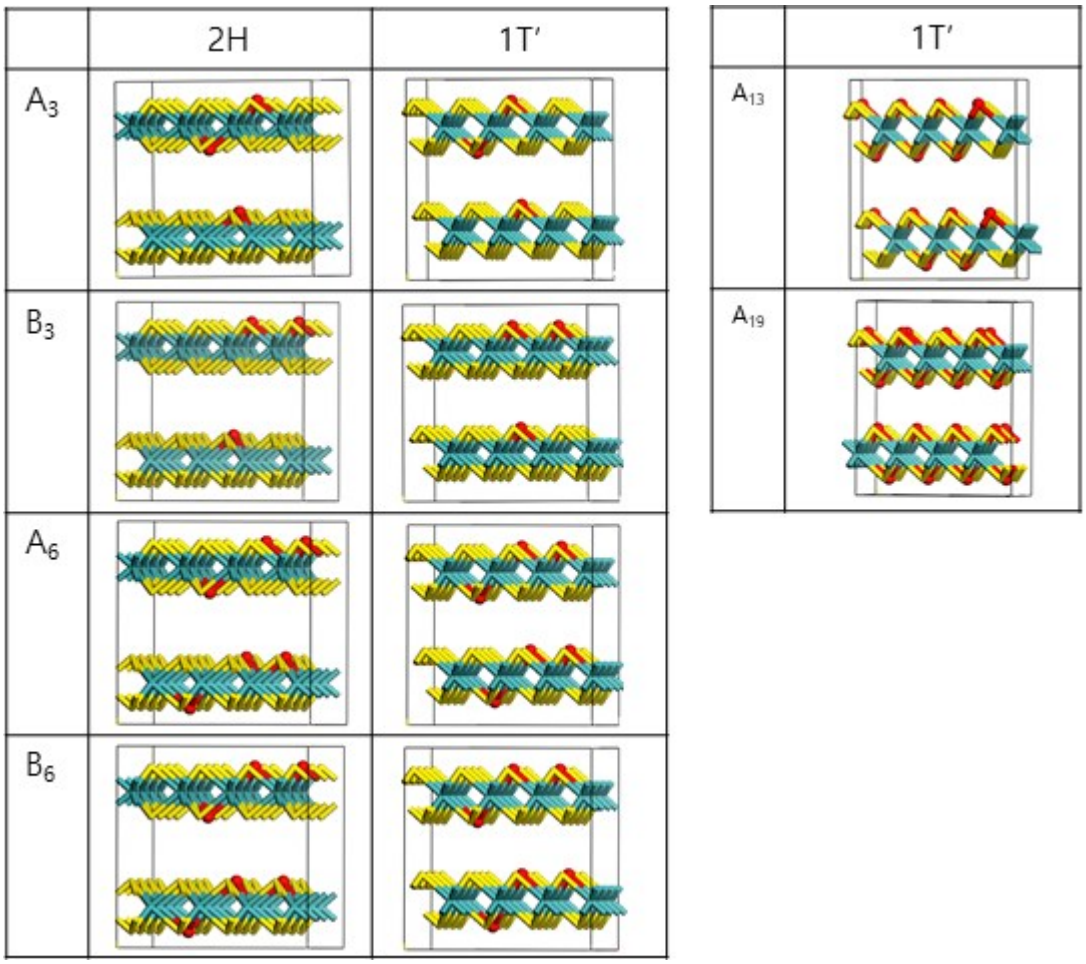

Figure S9. Structures of 2H- and 1T'-phase (4x4) MoS_2: A_3 and B_3 with N_{Vs} = 3; A_6 and B_6 with N_{Vs} = 6; 1T'-phase A_{13} with N_{Vs} = 13, and A_{19} with N_{Vs} = 19. For clarity, unit cells are shown along the *c* direction and vacancies are represented as red spheres.

Tables S3 compares the relative stabilities of various configurations of the defective (4×4) MoS_2 in the 2H and 1T' phases, containing various numbers of sulfur mono-vacancies (N_{Vs}). The vacancy concentration ranges from 4.7% to 29.7% per MoS_2 unit, corresponding to N_{Vs} = 3–19. For each N_{Vs} value, the most stable configuration (A_N) corresponds to the case in which the vacancies are randomly distributed in two MoS_2 layers in the supercell. In this regard, we note that each MoS_2 layer contains three sublayers, and vacancies can only be formed in the upper and lower sublayers (U_U, U_L, L_U, L_L) occupied by sulfur atoms. Here, U_U and U_L denote the upper and lower sublayers of the upper MoS_2 layer, respectively, whereas L_U and L_L represent the upper and lower sublayers of the lower MoS_2 layer. The second most stable configuration is referred to as B_N. The A_N configuration is more stable than the B_N one, irrespective of N_{Vs}, indicating that only A_N needs to be included in the additional investigations of DMPD intercalation in this work.

For both 2H and 1T' phases with $N_{Vs} = 3$, the B_3 configuration is characterized by two of the three vacancies concentrated on the same sublayer U_U of the same MoS_2 layer. However, two vacancies located on different sublayers of the same MoS_2 layer, (U_U, U_L) and (L_U, L_L), are two S-Mo bonds apart. This indicates that the two vacancies prefer to form virtual V_s^U-Mo-V_s^L bonds around the same Mo ion, in such a way that they belong to different sublayers. Based on this observation, configurations with higher vacancy concentrations are generated in such a way to include as many V_s^U-Mo-V_s^L motifs as possible.

Two V_s^U-Mo-V_s^L motifs are observed for $N_{Vs} = 6$, each located on a different layer. The different configurations can be further distinguished based on the relative arrangement of the two remaining S vacancies. In the A_6 and B_6 configurations, each vacancy is located four (V_s^U-Mo-S-Mo-V_s^U), two (V_s^U-Mo-V_s^U), and six virtual S-Mo bonds apart from one of the vacancies on the same sublayer, U_U and L_U. The A_6 configuration is significantly more stable than the B_6 one. In particular, B_6 is characterized by additional V_s^U-Mo-V_s^U virtual bonds, in such a way that the two V_s are located in the same sublayer. In summary, the rule of thumb is that the vacancies are arranged in order to achieve as many V_s^U-Mo-V_s^L and V_s^U-Mo-S-Mo-V_s^U motifs as possible, as well as shorter $l_{V_S-V_S}$ values (distances between the S vacancies at different MoS_2 layers).

The most stable configuration for $N_{Vs} = 13$, A_{13}, is characterized by 4, 3, 4, and 2 vacancies in the U_U, U_L, L_U, and L_L sublayers, respectively. In addition, the vacancies in the U_U and L_U sublayers are located in the V_s^U-Mo-S-Mo-V_s^U motifs, while vacancies in the U_L and L_L sublayers are built in such a way that as many V_s^U-Mo-V_s^L motifs as possible are present. When $N_{Vs} = 19$, there seems to be no way to avoid the V_s^U-Mo-V_s^U motifs within each sublayer, due to the high vacancy concentration. The most stable configuration (A_{19}) contains 6, 4, 5, and 4 vacancies located in U_U, U_L, L_U, and L_L sublayers, respectively. The other configurations present different numbers of vacancies in each sublayer as well as different interlayer-vacancy distances. Again, the A_{19} configuration exhibits the shortest $l(V_s\text{-}V_s)$ values among the three configurations considered.

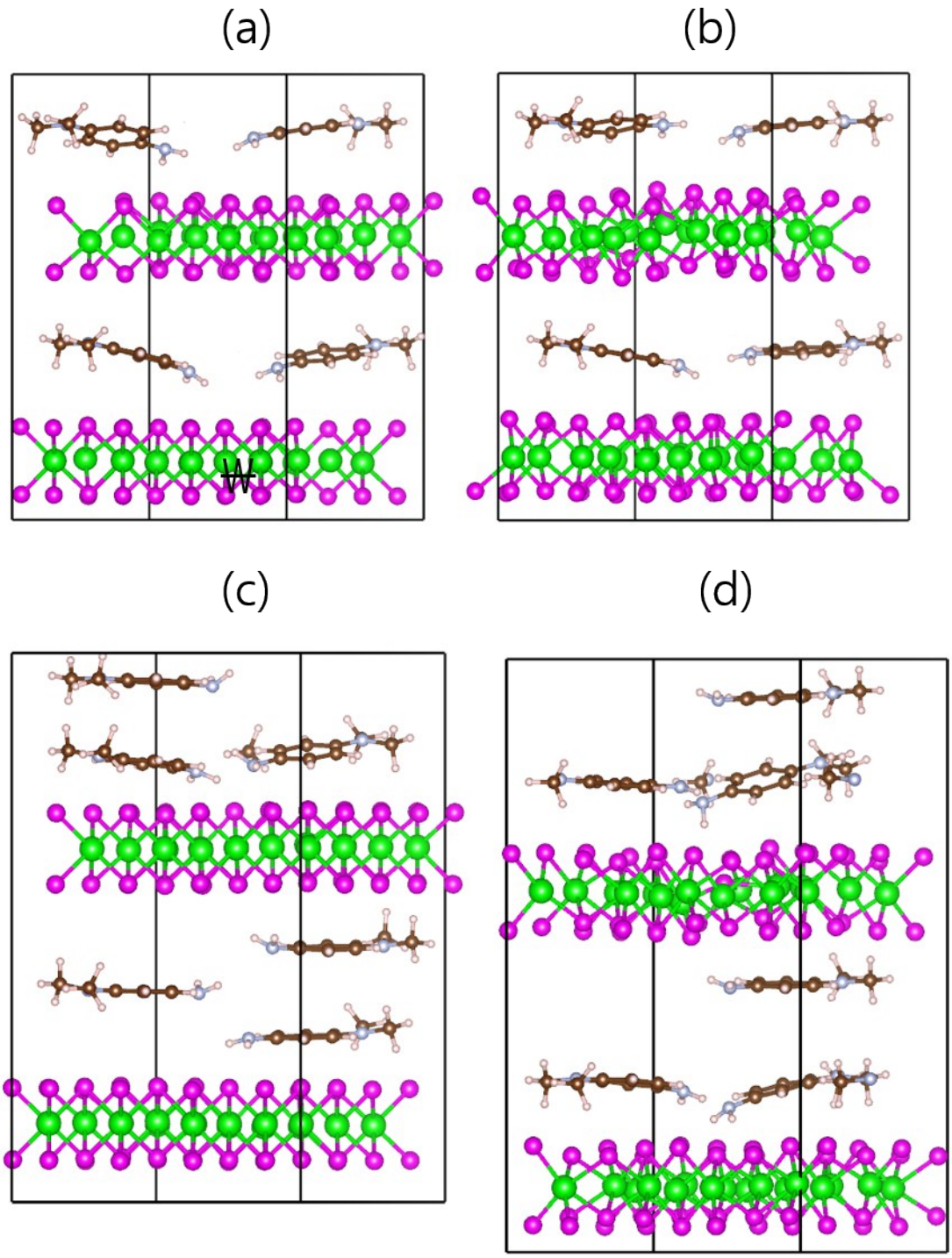

Figure S10. Structures of (a) 2H and (b) 1T' phases of (4×4) MoS_2-4DMPD ([DMPD] = 12.5%) at C_{Vs} = 20.3% and (c) 2H and (d) 1T' phases (4×4) MoS_2-6DMPD ([DMPD] = 18.8%) at C_{Vs} = 9.4%.

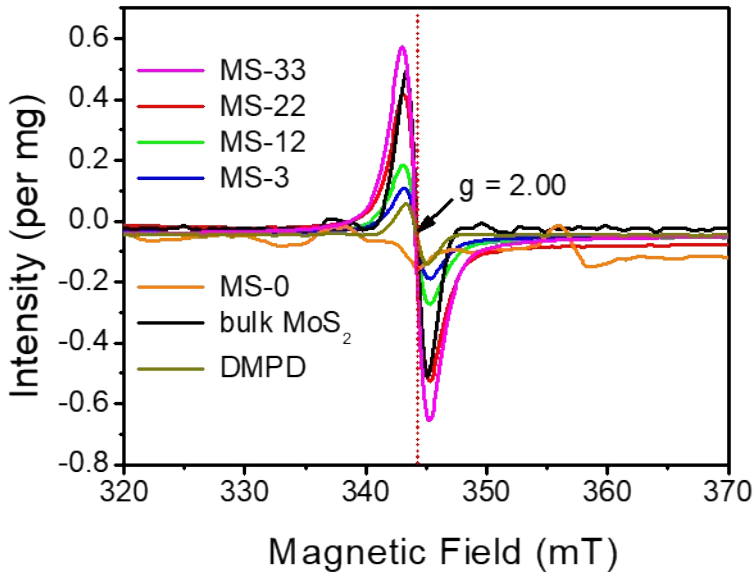

Figure S11. Electron spin (or paramagnetic) resonance spectra for (a) DMPD, MS samples, and bulk MoS_2.

ESR measurements were performed on a Bruker EMX-Plus spectrometer at room temperature. Ten milligrams of as-prepared samples were loaded in a quartz tube. The microwave frequency ν was 9.64 GHz (X-band), and the g-factor was calculated as $h\nu = g \times \mu_B \times B$, where μ_B and B are the Bohr magneton and magnetic field, respectively. Remarkably, the intercalated MoS_2 samples exhibit a strong S signal (per mg) at 344 mT (g = 2.00), and the intensity increases with increasing concentration of DMPD. Bulk MoS_2 exhibits a peak at g = 2.00, probably due to the S vacancies.[S22] However, the intensity of the intercalated MoS_2 samples is not correlated with the S vacancies; C_{Vs} = 13%, 25%, 8%, and 4% for MS-3, MS-12, MS-22, and MS-33, respectively. DMPD is widely used to measure the antioxidant potential of a sample; in the presence of Fe^{3+}, it is converted to the radical form, which is scavenged by antioxidant molecules present in test samples.[S23,S24] The peak of DMPD powders at g = 2.00 would be ascribed to the radical forms. Therefore, the signal of the intercalated MoS_2 can be originated from the radical form of DMPD. The results of the calculations indicate that the electron transfer from the DMPD molecules to MoS_2. The presence of DMPD radicals is probably indicative of an effective charge transfer to MoS_2.

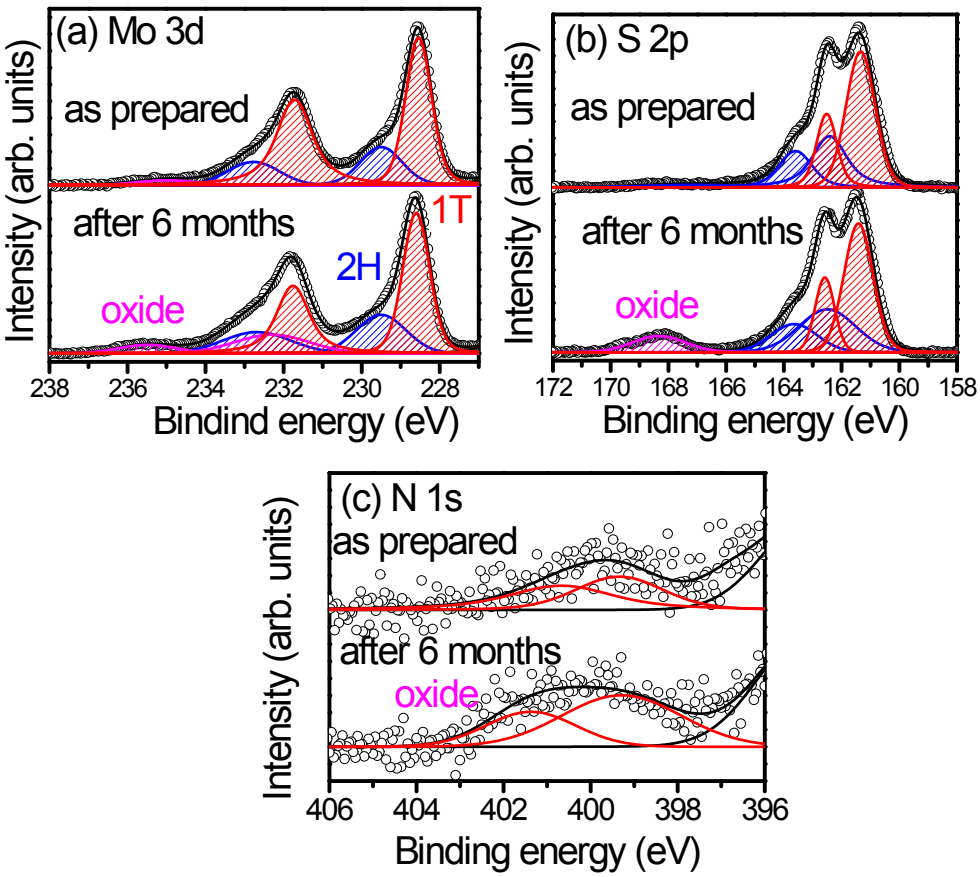

Figure S12. Fine-scan XPS peaks of (a) Mo 3d, (b) S 2p, and (c) N 1s for MS-12 before (as-prepared) and after 6 months. The 1T' phase and the DMPD content remain nearly constant after 6 months under ambient conditions, except for the formation of oxide layers at the surface.

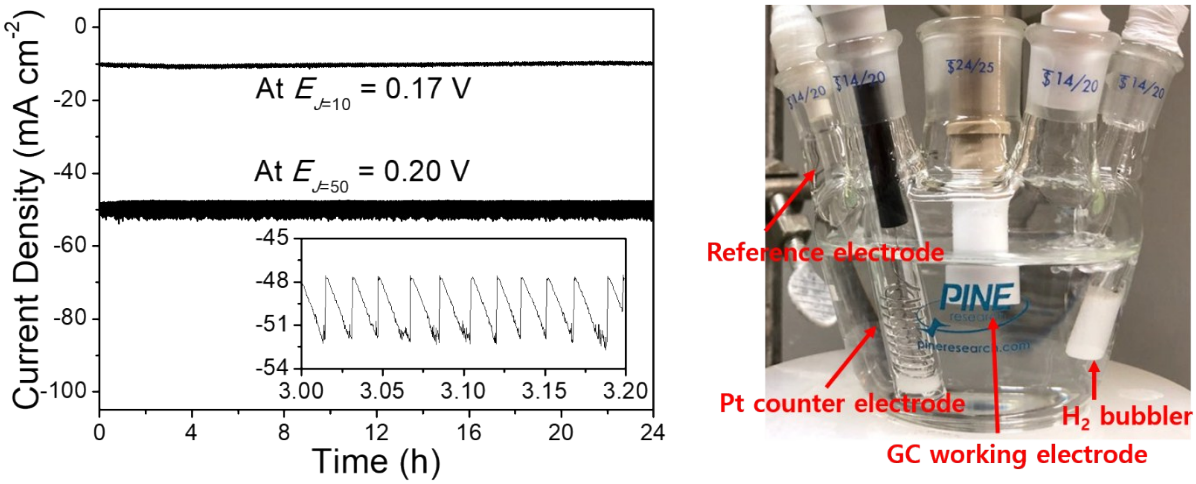

Figure S13. Chronoamperometric response (J vs. t) for the HER process using MS-3, at a constant applied potential of $E_{J=10}$ = -0.17 V and $E_{J=50}$ = -0.20 V vs. RHE. The current attenuation at 0.17 V is about 3% after 24 h, corresponding to the current density decreasing from 10.30 to 10.02 mA cm^{-2}. The I-t curve at -0.20 V also shows negligible attenuation with a typical serrate shape, which could be attributed to the alternate processes of bubble accumulation and bubble release. Photograph show the cell set up, showing that the Pt wire counter electrode was shielded by a membrane that block the transmission of the dissolved Pt ions into the electrolyte. Since the Pt ions didn't contaminate the electrolyte, no Pt deposition on the working GC electrode would occur.

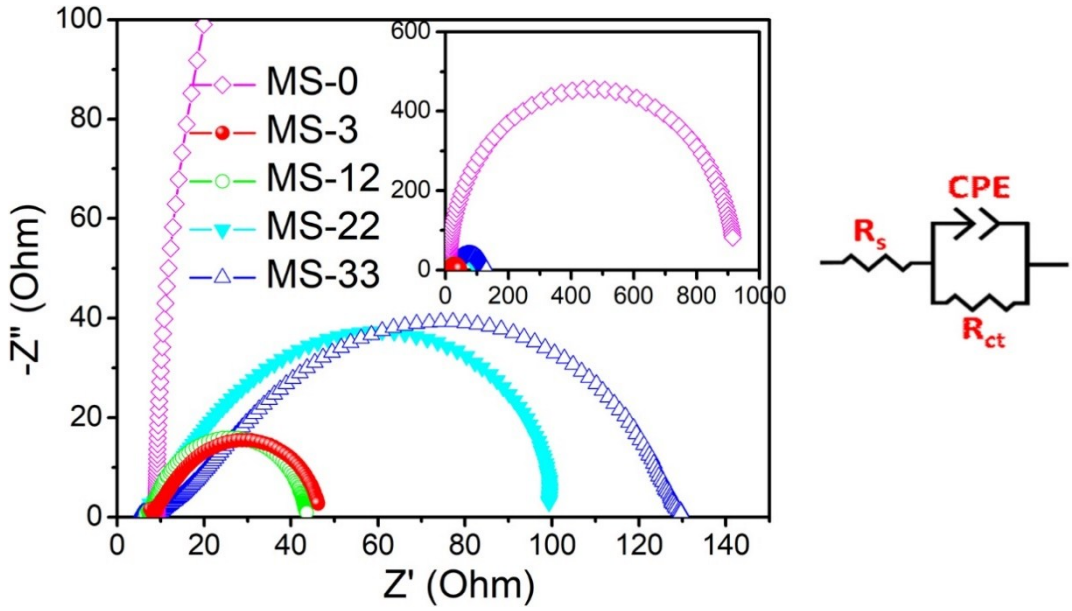

Figure S14. Nyquist plots for EIS measurements from 100 kHz to 0.1 Hz at a representative potential of -0.15 V (vs. RHE).

Electrochemical impedance spectroscopy (EIS) measurements of the samples were performed using a 100 kHz–0.1 Hz frequency range and an amplitude of 10 mV at $\eta = 0.15$ V. In the high-frequency limit and under non-Faradaic conditions, the electrochemical system is approximated by the modified Randles circuit shown on the right of Figure S15, where R_s denotes the solution resistance, CPE is a constant-phase element related to the double-layer capacitance, and R_{ct} is the charge-transfer resistance from any residual Faradaic processes. A semicircle in the low-frequency region of the Nyquist plots represents the charge transfer process, with the diameter of the semicircle reflecting the charge-transfer resistance. The real (Z') and negative imaginary ($-Z''$) components of the impedance are plotted on the x and y axes, respectively. The simulation of the EIS spectra using an equivalent circuit model allowed us to determine the charge transfer resistance, R_{ct}, which is a key parameter for characterizing the catalyst-electrolyte charge transfer process. The fitting parameters are listed in **Table S7**.

R_{ct} values of 910.8, 38.5, 36.5, 92.4, and 118.9 Ω were obtained for MS-0, MS-3, MS-12, MS-22, and MS-33, respectively, showing a sequence of MS-12 < MS-3 < MS-22 < MS-33 <

MS-0. The R_{ct} of the intercalated samples is much smaller than that of MS-0, indicating that the intercalation significantly reduces the charge-transfer resistance. The R_{ct} values follow an order consistently with the HER performance. The reduced charge-transfer resistance plays a major role in enhancing the HER catalytic activity of the DMPD-intercalated MS samples.

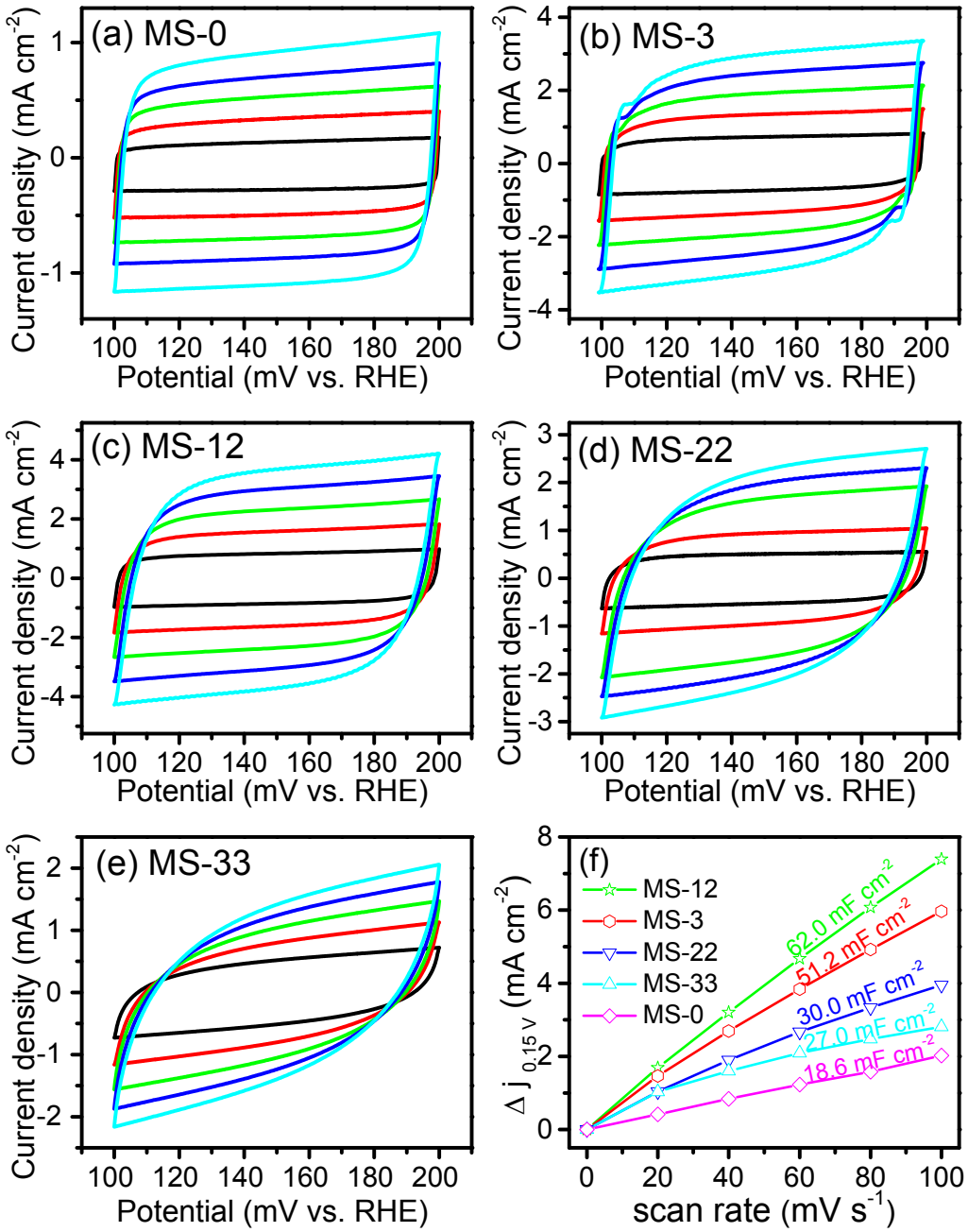

Figure S15. Cyclic voltammograms of (a) MS-0, (b) MS-3, (c) MS-12, (d) MS-22, and (e) MS-33 in a non-Faradaic region, at 20–100 mV s^{-1} scan rates and in 0.5 M H_2SO_4 solution. (f) Difference (ΔJ) between the cathodic discharging and anodic charging currents measured at 0.15 V (vs. RHE) plotted as a function of the scan rate (20, 40, 60, 80, and 100 mV s^{-1}).

Cyclic voltammograms were measured at 0.1-0.2 V, in a non-Faradaic region, using various scan rates. The double-layer capacitance (C_{dl}) was obtained as the slope of a linear fit of ΔJ vs. scan rate, where ΔJ is the difference between the cathodic discharging and anodic charging currents. The C_{dl} values of MS-0, MS-3, MS-12, MS-22, and MS-33 are 18.6, 51.2, 62.0, 30.0, and 27.0 mF cm^{-2}, respectively (see **Table S7**), showing a significant increase upon intercalation. The intercalated MoS_2 have high surface roughness and can thus expose a large number of active sites. The double-layer capacitance values follow the same order as the HER performance: MS-12 > MS-3 > MS-22 > MS-33 > MS-0. Therefore, the increased double-layer capacitance leads to the enhanced HER catalytic activity of the intercalated MS samples.

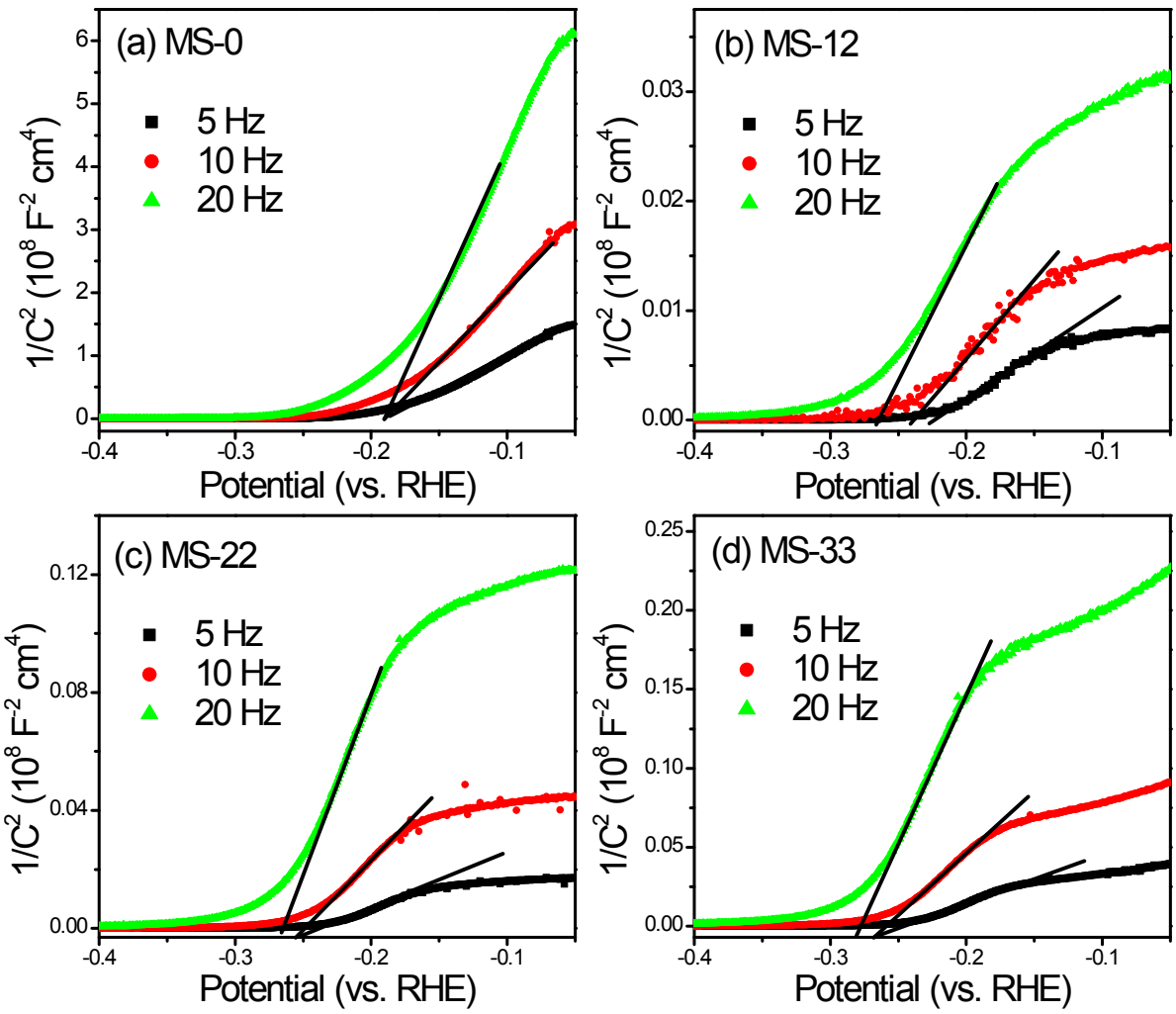

Figure S16. Mott-Schottky plots at 5, 10, and 20 Hz for (a) MS-0, (b) MS-12, (c) MS-22, and (d) MS-33. The experiments were conducted using 0.5 M H_2SO_4 as the electrolyte, a Pt wire as the counter electrode, and a saturated calomel (SCE) electrode as the reference electrode.

The Mott-Schottky plots were obtained by cathodically sweeping the potential with an AC amplitude of 10 mV. The collected data were analyzed using the Mott-Schottky equation $1/C^2 = 2/(\varepsilon\varepsilon_0 A^2 e N_D)(E - E_{fb} - k_B T/e)$, where C and A are the interfacial capacitance and the effective roughness factor (or interfacial area), respectively, ε is the dielectric constant of MoS_2, ε_0 is the permittivity of free space (8.85×10^{-12} J^{-1} C^2 m^{-1}), e is the electron charge (1.6×10^{-19} C), N_D is the number of carriers, E is the applied voltage, E_{fb} is the flat band potential, k_B is the Boltzmann constant, and T is the absolute temperature (K).

The straight lines represent fits of the linear regions of the Mott-Schottky plots. The flat band potentials were obtained from the intercepts of the fitted lines with the x-axis, giving E_{fb} values of -0.2 V for MS-0 and -0.25 V (on average) for MS-12, MS-22, and MS-33. Using the slope (k_{MS}) of the lines, the carrier concentrations in the samples were estimated as $N_D = 2(\varepsilon\varepsilon_0 A^2 e k_{MS})^-$

[1]. The dielectric constant of MoS_2 and the effective roughness factor were assumed to be 4 and 2, respectively, by approximating the nanosheets as spherical. The carrier concentrations were estimated to be 3.6×10^{19}, 7.4×10^{21}, 1.9×10^{21}, and 1.2×10^{21} cm^{-3}, respectively, for MS-0, MS-12, MS-22, and MS-33, using the data at 10 Hz. The carrier concentration of the intercalated samples is much larger than that of MS-0, indicating that the intercalation results in significantly higher carrier concentrations. The largest carrier density is found for MS-12, and decreases in the order MS-12 > MS-22 > MS-33, consistent with the HER performance. These results show that the increased carrier concentration determines the HER catalytic activity of the intercalated samples.

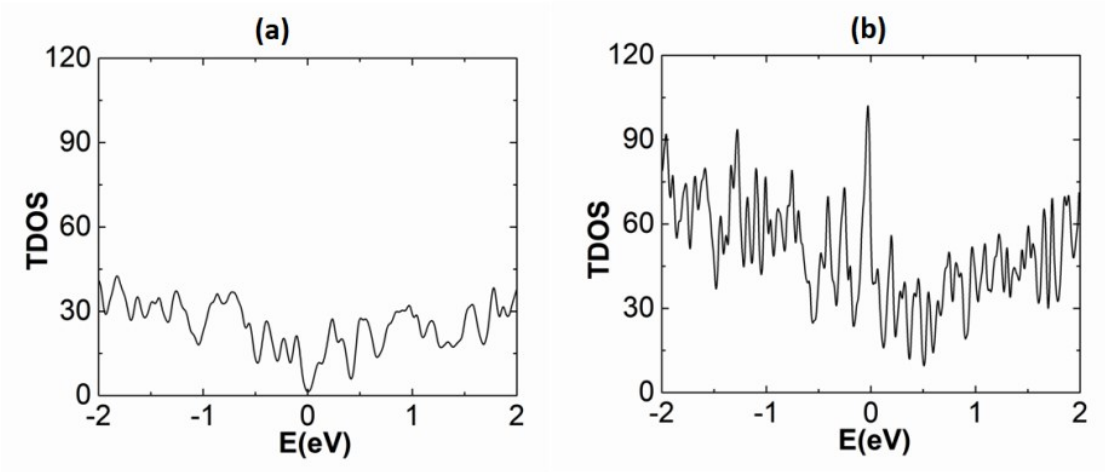

Figure S17. Total DOS of the 1T'-phase (a) (4×4) MoS_2 and (b) (4×4) MoS_2-4DMPD monolayers with C_{Vs} = 29.7%.

The 1T'-phase MoS_2 monolayer with C_{Vs} = 29.7% exhibits a finite DOS at the Fermi level. At this high concentration of S vacancies, MoS_2 adopts the 1T' phase. Compared to the DOS at C_{Vs} = 12.5% (shown in **Figure S18**), an appreciable increase in the DOS around the Fermi level (weighed by the Fermi-Dirac occupation) is observed. As DMPD molecules are intercalated, the DOS shows a substantial increase due to charge transfer from DMPD, which can enhance the catalytic efficiency toward the HER. In turn, the DOS increase will significantly enhance the cathodic current, relative to that originating from the S vacancies.

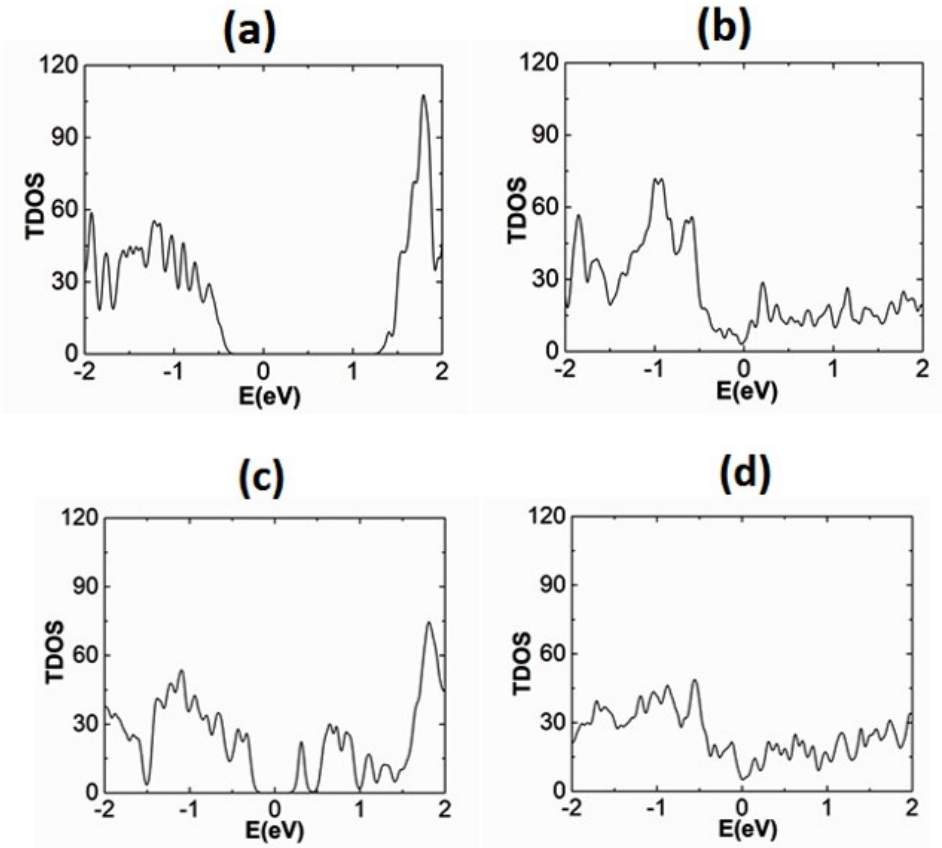

Figure S18. Total density of states (DOS) of the (a) 2H and (b) 1T' phases (4×4) MoS_2 monolayer with no S vacancies, and the (c) 2H and (d) 1T' phases (4×4) MoS_2 with four S vacancies (C_{Vs} = 12.5%).

Since the DMPD intercalation causes a significant expansion in the interlayer distances of MoS_2, direct interactions between the layers can be ignored. Therefore, the contribution of MoS_2 to the total DOS of the intercalated complex can be approximated as twice that of the MoS_2 monolayer. The 2H-phase MoS_2 monolayer displays a zero DOS at the Fermi level due to a significant band gap (1.68 eV) at C_{Vs} = 0%. The band gap decreases with increasing C_{Vs}, reaching 0.63 eV at C_{Vs} = 12.5%. The band gap (0.26 eV) of the 1T'-phase MoS_2 monolayer at the same C_{Vs} is significantly smaller.

IV. Reference

S1. H. L. Zhuan and R. G. Hennig, *J. Phys. Chem. C*, 2013, **117**, 20440.

S2. J. Xie, H. Zhang, S. Li, R. Wang, X. Sun, M. Zhou, J. Zhou, X. W. Lou and Y. Xie, *Adv. Mater.,* 2013*,* **25***,* 5807-5813.

S3. D. Voiry, M. Salehi, R. Silva, T. Fujita, M. Chen, T. Asefa, V. B. Shenoy, G. Eda and M. Chhowalla, *Nano Lett.,* 2013, **13**, 6222-6227.

S4. J. Xie, J. Zhang, S. Li, F. Grote, X. Zhang, H. Zhang, R. Wang, Y. Lei, B. Pan and Y. Xie, *J. Am. Chem. Soc.,* 2013, **135**, 17881-17888.

S5. M. Gao, M. K.Y. Chan and Y. Sun, *Nat. Commun.,* 2015, **6**, 7493.

S6. H. Li, C. Tsai, A. L. Koh, L. Cai, A. W. Contryman, A. H. Fragapane, J. Zhao, H. S. Han, H. C. Manoharan, F. A. Pedersen, J. K. Nørskov and X. Zheng, *Nat. Mater.,* 2015, **15**, 48-53.

S7. Z. Wu, C. Tang, P. Zhou, Z. Liu, Y. Xu, D. Wang and B. Fang, *J. Mater. Chem. A,* 2015, **3**, 13050-13056.

S8. D. Voiry, R. Fullon, J. Yang, C. C. C. Silva, R. Kappera, I. Bozkurt, D. Kaplan, M. J. Lagos, P. E. Batson, G. Gupta, A. D. Mohite, L. Dong, D. Er, V. B. Shenoy, T. Asefa and M. Chhowalla, *Nat. Mater.,* 2016*,* **15***,* 1003–1009.

S9. X. Geng, W. Sun, W. Wu, B. Chen, A. A. Hilo, M. Benamara, H. Zhu, F. Watanabe, J. Cui and T. Chen, *Nat. Commun.,* 2016, **7**, 10672.

S10. Y. Yin, J. Han, Y. Zhang, X. Zhang, P. Xu, Q. Yuan, L. Samad, X. Wang, Y. Wang, Z. Zhang, P. Zhang, X. Cao, B. Song and S. Jin, *J. Am. Chem. Soc.,* 2016, **138***,* 7965-7972.

S11. F. Z. Wang, M. J. Zheng, B. Zhang, C. Q. Zhu, Q. Li, L. Ma and W. Z. Shen, *Sci. Rep.,* 2016, **6***,* 31092.

S12. Y. Kim, D. H. K. Jackson, D. Lee, M. Choi, T. W. Kim, S. Y. Jeong, H. J. Chae, H. W. Kim, N. Park, H. Chang, T. F. Kuech and H. J. Kim, *Adv. Funct. Mater.,* 2017, **27**, 1701825.

S13. J. Zhang, J. Wu, H. Guo, W. Chen, J. Yuan, U. Martinez, G. Gupta, A. Mohite, P. M. Ajayan and J. Lou, *Adv. Mater.,* 2017*,* **29***,* 1701955.

S14. D. Wang, X. Zhang, S. Bao, Z. Zhang, H. Feia and Z. Wu, *J. Mater. Chem. A,* 2017, **5**, 2681–2688.

S15. Y. Shi, Y. Zhou, D. R. Yang, W. X. Xu, C. Wang, F. B. Wang, J. J. Xu, X. H. Xia and H. Y. Chen, *J. Am. Chem. Soc., 2017*, **139**, 15479-15485.

S16. E. E. Benson, H. Zhang, S. A. Schuman, S. U. Nanayakkara, N. D. Bronstein, S. Ferrere, J. L. Blackburn and E. M. Miller, *J. Am. Chem. Soc.,* 2018, **140***,* 441−450.

S17. C. Tan, Z. Luo, A. Chaturvedi, Y. Cai, Y. Du, Y. Gong, Y. Huang, Z. Lai, X. Zhang, L. Zheng, X. Qi, M. H. Goh, J. Wang, S. Han, X. Wu, L. Gu, C. Kloc and H. Zhang, *Adv. Mater*., 2018, **30***,* 1705509.

S18. Q. Liu, X. Li, Q. He, A. Khalil, D. Liu, T. Xiang, X. Wu and L. Song, *Small*, 2015, **11***,* 5556.

S19. S. S. Chou, S. Sai, P. Lu, E. N. Coker, S. Liu, K. Artyushkova, T. S. Luk, B. Kaehr and C. J. Brinker, *Nat. Commun.*, 2015, **6**, 8311.

S20. (a) D. Yang, S. J. Sandoval, W. M. R. Divigalpitiya, J. C. Irwin and R. F. Frindt, *Phys. Rev. B*, 1991, **43**, 12053. (b) S. J. Sandoval, D. Yang, R. F. Frindt and J. C. Irwin, *Phys. Rev. B*, 1991, **44**, 3955.

S21. J. Xie, J. Zhang, S. Li, F. Grote, X. Zhang, H. Zhang, R. Wang, Y. Lei, B. Pan and Y. Xie, *J. Am. Chem. Soc.*, 2013, **135**, 17881.

S22. B. Deroide, Y. Bensimon, P. Belougne and J. V. Zanchetta, *J. Phys. Chem. Solids*, 1991, **52**, 853.

S23. K. Hirayama and N. Unohara, *Anal. Chem.*, 1988, **60**, 2573.

S24. M. M. Mehdi and S. I. Rizvi, *Anal. Biochem*., 2013, **436**, 165.